Pergamon

PII: S0021-8502(00)00042-2

www.elsevier.com/locate/jaerosci

J. Aerosol Sci. Vol. 31, No. 12, pp. 1447–1460, 2000

Printed in Great Britain
0021-8502/00/$ - see front matter

DROPLET DISTORTION IN ACCELERATING FLOW

D. L. Bartley,*† A. B. Martinez,† P. A. Baron,† D. R. Secker‡ and E. Hirst‡

†Centers for Disease Control and Prevention, National Institute for Occupational Safety and Health, Cincinnati, OH 45226, U.S.A
‡Particle Instruments Research Group, Science and Technology Research Centre, University of Hertfordshire, College Lane, Hatfield, Hertfordshire AL109AB, U.K.

(*First received* 8 *March* 2000; *and in final form* 13 *March* 2000)

Abstract—Several commercial instruments size particles based on their acceleration in a high-velocity flow field. Previous work suggested that droplet distortion in these instruments resulted in inaccurate sizing. Liquid aerosol droplet shape distortion produced in an accelerating flow field was therefore computed through analytical solution of the Navier–Stokes equation for comparison to experiment. A high-Reynolds-number empirical approximation to the pressure external to the droplet was used in these calculations. Within the droplet, the longest-lived excitations correspond to a quadrupolar distortion of shape. Droplet excitations were obtained in terms of aerosol diameter, viscosity, surface tension and density. At the largest viscosities considered (as in many oils), only a damped relaxation was found, whereas at lower viscosities and high surface tension (as in water) damped capillary oscillations were predicted as possible, given rapid shifts in the surrounding air flow. In order to compute the effect of airflow varying in time, an approximate Green's function was used. The Green's function in the frequency domain was approximated using only a pair of poles, thereby accounting for only the longest-lived excitations. In application of the theory to compute aerosol distortion on passage through an aerodynamic particle sizer (APS) acceleration nozzle, the change in air velocity was found to be so gradual that no oscillations were induced for droplets as small as 20-μm diameter. Measurements of droplet undersizing in the APS compared favorably with the theoretical predictions. The theoretical results were also consistent with photographs of distorted oleic acid and only slightly distorted water droplets emerging from a nozzle.

1. INTRODUCTION

Accurate, real-time measurement of aerosol particle aerodynamic size is useful for a variety of applications including measurement of environmental aerosols (Sioutas *et al*., 1999), testing cyclones (Maynard and Kenny, 1995) and measurement of airborne bacterial size (Madelin and Johnson, 1992; Ho, 1996). Several instruments are commercially available for real-time measurement of particle aerodynamic diameter including the SPART (Hosakawa Micron International, Osaka), three versions of the Aerodynamic Particle Sizer (APS 3310, APS 3320, UV-APS3312A, TSI, Inc. St. Paul, MN), the Aerosizer (TSI, Inc. St. Paul, MN) and the aerosol time-of-flight mass spectrometer (Model 3800, TSI, Inc. St. Paul, MN). Excluding the SPART, these instruments size particles by accelerating them in a nozzle and measuring the particle velocity to estimate aerodynamic diameter. This approach has advantages in providing rapid measurements, but has several potential drawbacks as well. One of the drawbacks is that liquid droplet measurements may be biased because the droplet acceleration through the nozzle can cause significant distortion of the droplet shape, resulting in inaccurate measurement of droplet size (Baron, 1986; Griffiths *et al*., 1986). If the droplet distortion can be predicted based on liquid properties such as viscosity, density and surface tension, more accurate measurement of droplet size can be made. The work described below represents an approach to calculating droplet deformation in an accelerating flow field and estimating the effect on APS-measured size.

Within the following sections, the longest-lived modes of droplet oscillation and relaxation are initially considered for the case that the pressure external to the droplet is constant. In some situations, the simplest mode consists in the longest possible wavelength

*Author to whom correspondence should be addressed.

capillary waves circling the droplet. In others, only a relaxation to spherical shape occurs. This theory is then expanded to account for time-dependent external pressure varying along the droplet surface. The increased air speed on moving along the droplet surface from pole to equator corresponds to an azimuthal lift, resulting in droplet distortion or flattening perpendicular to the axis of the nozzle. Explicit expressions for drag, pressure and air velocity in the APS nozzle then permit calculation of the time-dependent distortion and particle velocity. Finally, calculation is compared to experiments consisting of both laser imaging of particles exiting the nozzle and APS-measured sizes of a variety of liquid droplets.

2. FUNDAMENTAL OSCILLATION/DECAY MODES

2.1. *Overview*

The longest-lived polar-symmetric excitations of small droplets of radius a are investigated here in terms of surface tension σ, viscosity η and density ρ. Considered first is the case that the external pressure around the droplet is constant, spatially and temporally. Induction of these excitations by the changing pressure in an accelerating air stream is then taken up in Section 3. A dimensionless constant β defined by

$$\beta = a\rho\sigma/\eta^2 \tag{1}$$

is found to characterize the form of excitation. Table 1 lists the physical constants of interest for several liquids for comparison.

At $\beta \gg 1$, the restoring surface tensions dominate dissipative viscous effects. Droplet oscillations correspond in this case to the longest-possible-wavelength capillary waves capable of circling a sphere that result in a standing wave. At small amplitudes, the droplet oscillates approximately between prolate and oblate spheroidal shapes. The angular oscillation frequency ω is

$$\omega = [8/\beta]^{1/2} \times [a\eta/\sigma]^{-1}, \quad \beta \gg 1. \tag{2}$$

The damping of this type of excitation is found to agree with a calculation published by Landau and Lifshitz (1959, p. 240) translated from planar to spherical geometry, namely, exponential damping with lifetime τ_{relax}:

$$\tau_{\text{relax}} = \beta/5 \times [a\eta/\sigma], \quad \beta \gg 1. \tag{3}$$

Decreasing β corresponds to increased dissipation as viscous effects overwhelm the restorative surface tension. In fact, at a critical value of β approximately equal to 1.7, the frequency $\omega \to 0$, and damping dominates. At $\beta \ll 1$, no oscillation is possible (similar to an overdamped harmonic oscillator); only a purely exponential relaxation towards spherical shape occurs, with a characteristic time τ_{relax} given by

$$\tau_{\text{relax}} = 19/20 \times [a\eta/\sigma], \quad \beta \ll 1. \tag{4}$$

Table 1. Properties of investigated liquids at 20°C

Liquid	Surface tension, σ (kg s^{-2})	Viscosity, η (Pa s)	Density, ρ (kg m^{-3})	β (at $D_{ae} = 15$ μm)
Oleic acid	0.032	0.0256	894	0.35
DC 200/50	0.0208	0.050	960	0.062
DC 200/100	0.0209	0.10	964	0.016
DC 200/200	0.0210	0.20	967	0.0039
DC 200/500	0.0211	0.50	969	0.00062
Water	0.0727	0.0010	1000	547

2.2. *Calculation*

Details of the longest-lived droplet excitations are obtained as follows. The fluid obeys a mass-conserving continuity equation and also the Navier–Stokes equation, describing the effect of forces associated with internal pressure p and viscosity. Linear approximation to the Navier–Stokes equation is accurate because of the small velocities (and gradients) relative to the droplet center. Conservation of mass is guaranteed for an incompressible fluid, together with azimuthal symmetry (about the z-axis taken to lie along the axis of the APS nozzle), by expressing the fluid velocity $\mathbf{v}$ in terms of potentials Φ and Φ_{irr} by

$$\mathbf{v} = \text{curl}\,[\nabla\Phi \times \hat{k}\,] + \nabla\Phi_{\text{irr}}, \tag{5}$$

where $\hat{k}$ is a unit vector along the z-axis. The second term includes an irrotational component to the fluid's motion via Laplace's equation

$$\Delta\Phi_{\text{irr}} = 0. \tag{6}$$

Assuming that the velocity is proportional to $\exp(-t/\tau)$, where τ is a complex relaxation time (s), the Navier–Stokes equation is

$$-\frac{\rho}{\tau}\,\mathbf{v} = -\nabla p + \eta\Delta\mathbf{v}. \tag{7}$$

Substituting the velocity $\mathbf{v}$ (equation (5)) into the Navier–Stokes equation then results in an equation for the potential Φ

$$\Delta\Phi = -\frac{1}{v\tau}\,\Phi, \tag{8}$$

where v is the kinematic viscosity η/ρ.

The potential is found by expanding in Legendre polynomials $P_l[\cos\,[\theta]]$, remembering that only solutions with azimuthal symmetry are sought. Therefore, equation (8) is solved by

$$\Phi = \Phi_l[r]\,P_l[\cos\,[\theta]]\exp\,[-t/\tau], \tag{9}$$

where $\Phi_l[r]$ obeys

$$\ddot{\Phi}_l + \frac{2}{r}\,\dot{\Phi}_l + \left[\frac{1}{v\tau} - \frac{l(l+1)}{r^2}\right]\Phi_l = 0. \tag{10}$$

Equation (10) is solved in terms of spherical Bessel functions j_l (Abramowitz and Stegun, 1965)

$$\Phi_l \propto j_l[r/\sqrt{v\tau}]. \tag{11}$$

As $l = 0$ corresponds simply to the droplet translating uniformly along the z-axis, the lowest value of l of interest is the term with $l = 1$, where

$$P_1[\cos\theta] = \cos\theta, \tag{12}$$

$$j_1[w] = \frac{\sin w}{w^2} - \frac{\cos w}{w}, \tag{13}$$

where w is the argument of the spherical Bessel function, as in equation (11). Similarly, the lowest term of interest in Φ_{irr} is the quadrupole term

$$\Phi_{\text{irr}} \propto r^2 P_2[\cos\theta], \tag{14}$$

where

$$P_2[\cos\theta] = \tfrac{1}{2}\,(3\cos^2\theta - 1). \tag{15}$$

Higher-order terms corresponding to shorter wavelength capillary waves will have shorter relaxation times, and, though of interest, are neglected here relative to the dominant oscillation mode.

Superposing the rotational and irrotational components of the velocity field using constants α and $\alpha_{\rm irr}$ results in the following expressions (omitting the exponential time dependence) for the radial and angular velocities, v_r and v_θ:

$$v_r = \left\{\alpha\,\frac{j_2[r/\sqrt{\nu\tau}]}{r} - \alpha_{\rm irr} r\right\}[3\cos^2\theta - 1] \tag{16}$$

$$v_\theta = \left\{\alpha\,\frac{j_3[r/\sqrt{\nu\tau}]}{\sqrt{\nu\tau}} - 3\alpha\frac{j_2[r/\sqrt{\nu\tau}]}{r} + \alpha_{\rm irr} 3r\right\}[\cos\theta\sin\theta]. \tag{17}$$

The pressure p inside the droplet near $r = a$ can now be obtained from the Navier–Stokes equation (7) as

$$p = -\,\alpha_{\rm irr}\,\frac{\rho a^2}{2\tau}\,[3\cos^2\theta - 1]. \tag{18}$$

Similarly, the deviation ζ of the free surface from $r = a$ is determined by requiring $\mathrm{d}\zeta/\mathrm{d}t = v_r$ near $r = a$

$$\varsigma = \tau\,\left\{-\,\alpha\,\frac{j_2[a/\sqrt{\nu\tau}]}{a} + \alpha_{\rm irr} a\right\}[3\cos^2\theta - 1]. \tag{19}$$

Therefore, at small distortion, the droplet approximates the shape of an ellipsoid. At larger distortions, the droplet is more toroidal in shape.

Following Landau and Lifshitz (1959, pp. 230–234), the change $\delta(1/a_{\rm c})$ in the curvature (twice the reciprocal of the geometric mean of the surface's local principal radii) from $2/a$ is given by

$$\begin{aligned}\delta(1/a_{\rm c}) &= -\,2\zeta/a^2 - \Delta\zeta \\ &= 4\zeta/a^2,\end{aligned} \tag{20}$$

which is determined directly by expression (19) for ζ. The curvature, multiplied by the surface tension, gives the pressure just inside the droplet surface.

The constants α and $\alpha_{\rm irr}$ are determined by requiring the forces at the droplet surface to be sensible. Namely, the fluid stress tensor component $\sigma_{r\theta}$ parallel to the surface must vanish, whereas the stress σ_{rr} normal to the surface must match the induced surface tension pressure and pressure $p_{\rm ext}$ external to the droplet

$$\sigma_{r\theta} = \eta\left[\frac{1}{r}\,\frac{\partial v_r}{\partial\theta} + \frac{\partial v_\theta}{\partial r} - \frac{v_\theta}{r}\right] = 0, \tag{21}$$

$$\sigma_{rr} = -\,p + \frac{\sigma}{a_{\rm c}} + 2\eta\,\frac{\partial v_r}{\partial r} = -\,p_{\rm ext}. \tag{22}$$

In the case that the external pressure $p_{\rm ext}$ is zero, substituting the expressions found for v_r, v_θ, p, and ζ results in two homogeneous linear equations in α and $\alpha_{\rm irr}$. Existence of non-trivial solutions then requires that the equation set's (secular) determinant vanish

$$\det = \left\|\begin{matrix} \dfrac{w^2}{2} - 2 + 4\,\dfrac{\beta}{w^2} & \dfrac{6j_1}{w} - \dfrac{24j_2}{w^2} - \dfrac{12\beta j_2}{w^4} \\ 1 & \left(-\dfrac{8}{w^2} + \dfrac{1}{2}\right)j_2 + \dfrac{j_1}{w} \end{matrix}\right\| = 0, \tag{23}$$

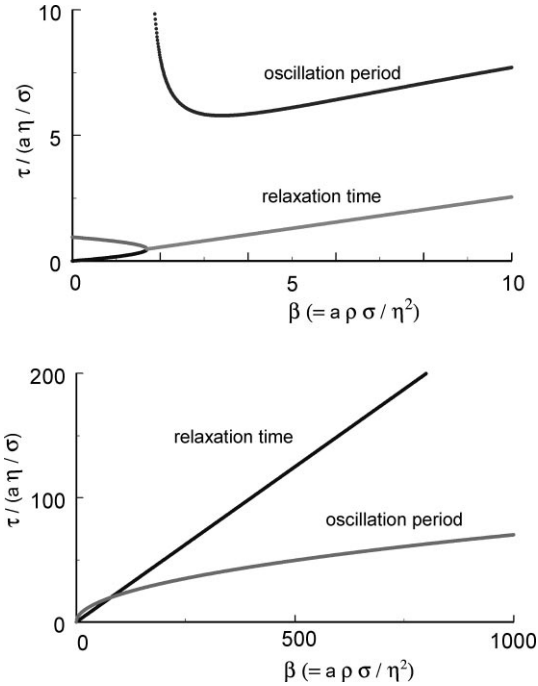

Fig. 1. Oscillation period and relaxation times of a liquid aerosol to spherical shape.

where w is the argument of the spherical Bessel functions at $r = a$

$$w = a/\sqrt{v\tau}. \tag{24}$$

By expansion of the spherical Bessel functions, solution of equation (23) is possible analytically in the limits, $\beta \to 0$, and $\beta \to \infty$, and results in the frequency and damping times given in equations (2)–(4). For intermediate cases, however, equation (23) results in a transcendental equation that can only be solved numerically. The result for the longest-lived excitations is shown in Fig. 1. An interesting feature is that when β is approximately equal to 1.7, the oscillation frequency approaches zero.

3. DISTORTION BY TIME-DEPENDENT EXTERNAL PRESSURE

3.1. *Quadrupolar-projected external pressure*

The above results can be applied to the estimation of effects of a varying external pressure p_{ext} on a droplet. More accurately, as only the quadrupolar excitations (i.e. proportional to $[3\cos^2\theta - 1]$) are of interest, the effect of the quadrupolar projection of the external pressure, azimuthally symmetric, is approximated. In other words, $p_{\text{ext}}[\theta]$ is expanded as

$$p_{\text{ext}}[\theta] = \sum_{l=1}^{\infty} p_l P_l[\cos\theta], \tag{25}$$

$$p_l = \frac{2l+1}{2}\int_0^{\pi} \sin\theta \, \mathrm{d}\theta \, p_{\text{ext}}[\theta] P_l[\cos\theta]. \tag{26}$$

Then the $l = 2$ projected pressure p_{ext} is

$$p_{\text{ext}} = p_2 \tfrac{1}{2}(3\cos^2\theta - 1), \tag{27}$$

where p_2 is, in general, time-dependent. The effect of pressure projections of higher order than $l = 2$ is neglected here, as their damping is stronger than the $l = 2$ term, which would therefore generally dominate if present.

3.2. *Approximate Green's function solution for droplet distortion at time t*

Equations (21) and (22) must now be solved in the case that the external pressure p_{ext} is not zero and may induce droplet excitation. The determinant of equations (21) and (22) does not now vanish, but its reciprocal is approximated as a function of complex frequency with only two poles, at the complex excitation frequencies determined as above, numerically, from equation (23). In other words, only the longest-lived excitations are accounted for. Formally, given the Fourier transform $p_2(\omega)$ at frequency ω, the linear algebraic equations (21) and (22) are solved for α and α_{irr}, i.e., for the Fourier-transformed distortion ζ. Transforming back to the time domain then gives the time-dependent $\zeta(t)$ in terms of a Green's function $G(t - t')$ in the form

$$\zeta(t) = \int_0^t \mathrm{d}t' G(t - t') p_{ext}(t'). \tag{28}$$

The time dependence of G is very simple in the longest-lived pole approximation adopted here. For example, as β (of equation (1)) approaches zero, which occurs for large viscosity, small size, or small surface tension

$$G \propto \exp\,[-(t - t')/\tau]. \tag{29}$$

On the other hand, if β is large enough that damped oscillatory excitations are possible, then two terms in G are significant, proportional to $\exp\,[-\mathrm{i}\omega_{cap}(t - t')]$ and its complex conjugate, where ω_{cap} is the complex spherical capillary wave oscillation frequency described above via equations (2) and (3). In either case, the integral of equation (28) can be computed numerically, using an explicit form for the quadrupolar approximation of the external pressure $p_{ext}(t)$.

4. DRAG AND EXTERNAL PRESSURE DISTRIBUTION

4.1. *Accelerating drag on droplets*

For calculating particle trajectories, x vs time t, the following or equivalent expression (Klyachko, published by Fuchs, 1964) for the force must be used, since particle Reynolds numbers >1 prevail throughout much of the motion through the nozzle:

$$F_{drag} = 6\pi\eta_{air} a'(v_{air} - v)[1 + \tfrac{1}{6}\mathrm{Re}^{2/3}]. \tag{30}$$

The quantities a' and the Reynolds number Re refer to the distorted major axis radius of the aerosol. The first term in the brackets gives the small-Reynolds-number Stokes force on a particle; the second corrects for higher air velocity relative to the particle.

4.2. *Distorting pressure near the aerosol surface*

At low Reynolds numbers, the pressure near the particle is approximately equal to the pressure in an irrotational fluid near an ellipsoid (Lamb, 1945). However, at the high Reynolds numbers (up to about 100) of greater significance here, air circulation is significant near a particle's downstream surface. This results in two effects (Landau and Lifshitz, 1959; Schlichting, 1979):

(1) the pressure drops along the upstream surface from pole to equator, but is essentially constant along the downstream surface, and

(2) the pressure difference between upstream and downstream surfaces accounts for a so-called particle *form-drag*, which dominates over the viscous drag of air flowing next to the particle's surface.

These effects are expressed here as follows. The pressure $p_{\text{ext}}(\theta)$ at angle θ relative to the upstream pole is modeled as

$$p_{\text{ext}}(\theta) = A + B \left\{ \begin{array}{ll} \cos^2\theta, & 0 < \theta < \pi/2, \\ \text{else}, & 0 \end{array} \right\}. \tag{31}$$

The constant A contributes neither to the form-drag nor to distortion of the droplet. The constant B contributes to both and is determined so as to recover equation (30) by integration. The result for the quadrupolar projection p_2 of the pressure along the surface is

$$p_2 = \frac{2F_{\text{drag}}}{3\pi a^2}, \tag{32}$$

where a is again the undistorted droplet radius.

It is now straightforward to compute particle trajectories through the nozzle, given the air velocity as a function of distance. For the nozzle used in the various current models of the APS, the air velocity v_{air} along the nozzle axis has been modeled using computational fluid dynamics (CFD) (Ananth and Wilson, 1988) with results shown in Fig. 2. Also shown in Fig. 2 is the trajectory calculated using equation (30) for a 20-μm 10^3 kg m^{-3} solid aerosol particle. Of interest is the aerosol velocity at position $x = 500\,\mu$m, where the aerosol's velocity on exiting the nozzle is measured in the APS.

Calculated velocities for *liquid* aerosols in this sensing region are computed as follows. The aerosol velocity $v(t)$ (or equivalently at position x) is determined by numerical integration of Newton's second law over times $t' < t$, using the force F_{drag} given in equation (30). F_{drag}, required at each value t', is itself the result of numerical integration, using equation (28), since the Green's function G (through equation (32) and F_{drag} at t' both depend on the aerosol distortion and the aerosol velocity itself. The two integrations are straightforward numerically using a 400 MHZ PC and are carried out coincidentally.

The calculated liquid aerosol velocity at $x = 500\,\mu$m is then compared to velocities of solid aerosols of the same density and with diameters in the neighborhood of the liquid aerosol. The final result is an estimate of the undersizing expected of the APS in measuring

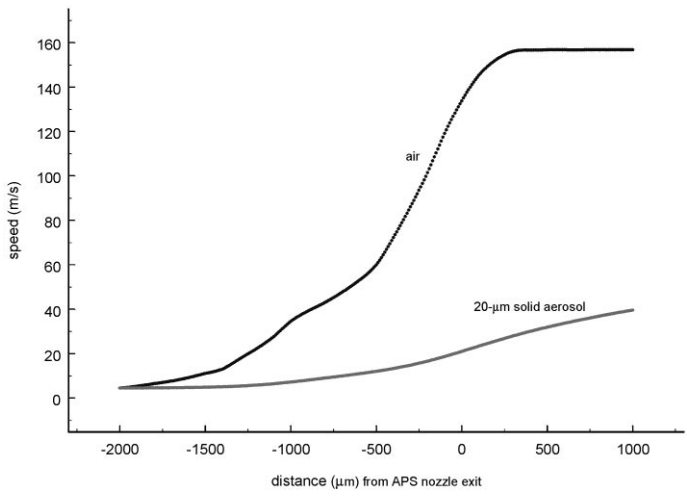

Fig. 2. Velocity of air (from calculation of velocity by Ananth and Wilson (1988)) and 20-μm solid 10^3 kg m^{-3} particles through APS nozzle.

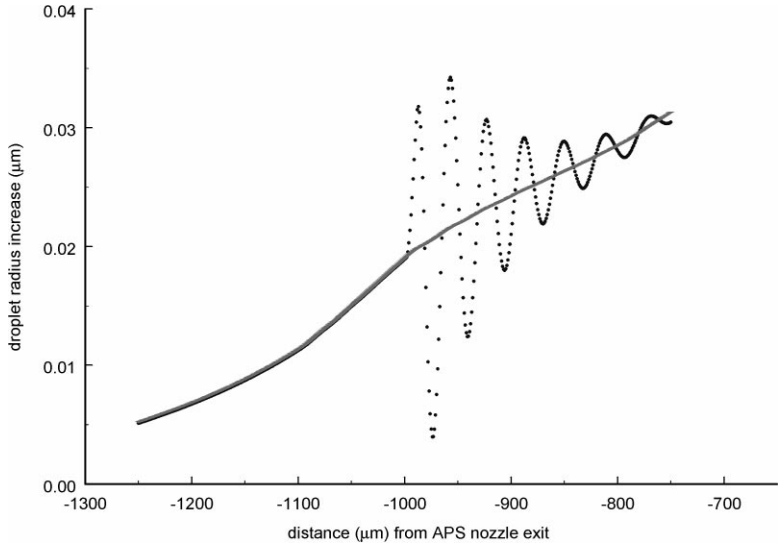

Fig. 3. Damped capillary oscillation induced by single-wavelength square wave superimposed on normal surrounding air flow in APS nozzle. A 10-μm water droplet's major semi-axis increase over initial radius is plotted. The solid curve represents non-oscillatory distortion expected with the gradual air flow increase of normal nozzle operation.

a liquid aerosol of given diameter, density, surface tension and viscosity. Results of this calculation are given below, together with corresponding experimental values, in terms of the deviation between APS-measured diameter and aerodynamic diameter.

One result of interest here, however, is the theoretical prediction that the air velocity through the APS nozzle increases sufficiently gently that no oscillations are induced. Consider, for example, the case of water droplets for which the surface tension is large enough that capillary oscillation is physically possible (see the dimensionless parameter β of equation (1) and Table 1). Figure 3 shows the acceleration of an 10-μm water droplet. For illustration a single-period square wave of amplitude 5 m s^{-1} and length 20 μm was superimposed on the APS nozzle air flow. Note the induced oscillations and their rapid damping.

5. EXPERIMENTAL

5.1. *Droplet imaging*: *Oleic acid*

Images of oleic acid droplets were obtained using an APS nozzle subassembly and a pulsed laser imaging system. A photomultiplier tube (PMT) was used to determine when a droplet was in the measurement space. This PMT signal was coupled into an electronic signal generator, which in turn provided a trigger signal for a pulsed 15 W copper vapor laser (CVL). The CVL light was coupled to a 1-mm diameter fiber optic cable. The other end of the fiber was positioned behind a diffuser to provide a uniform background illumination to enable a flash shadow micrograph of the droplet to be obtained. A high-resolution CCD camera coupled via a $\times 10$ microscope objective was used to image the droplets. The size of the array and optics gave an effective pixel resolution of 0.67 μm in the image plane.

The edges of the droplets were determined by processing the acquired images on a PC using a Gaussian edge detection algorithm in Matlab software (Mathworks, Natick, MA). The output gives a binary file image which can then in turn be used to obtain the diameter of the droplet.

The undistorted (spherical) diameter was calculated from the fundamental vibrating orifice aerosol generator (VOAG, TSI, Inc., St. Paul, MN).) disturbance frequency. The result was a 19.4-μm aerodynamic diameter droplet.

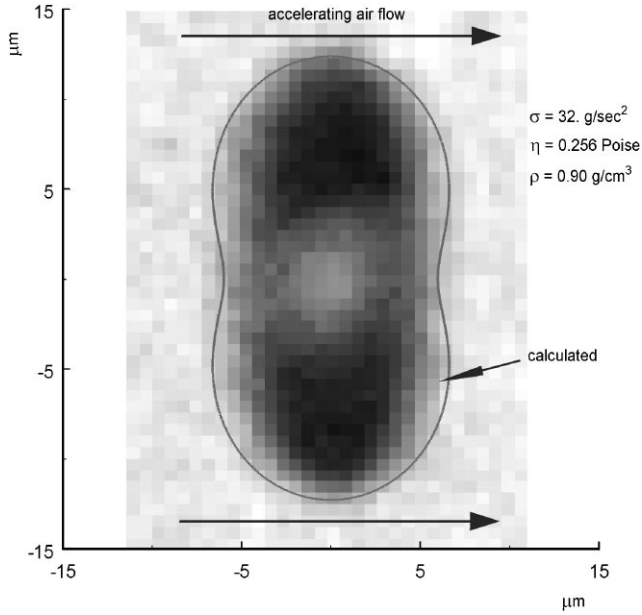

Fig. 4. Comparison of laser-imaged and calculated 19.4-μm oleic acid droplet.

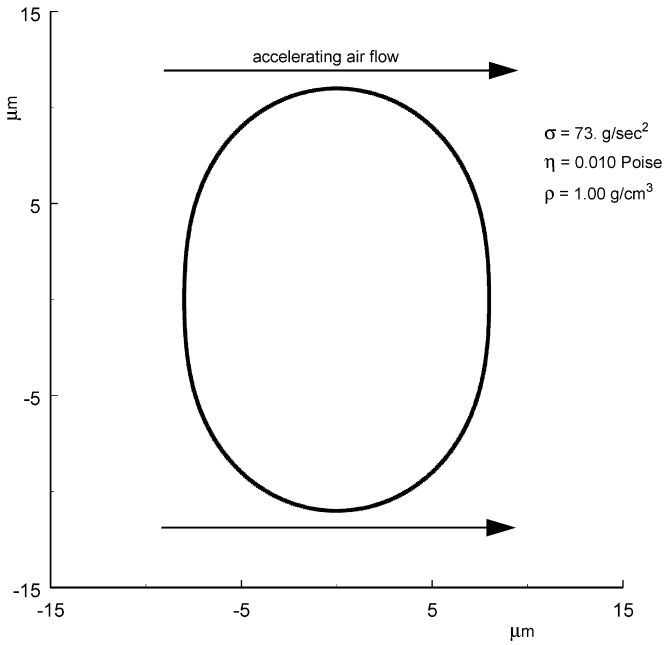

Fig. 5. Calculated shape of 20-μm water droplet in the measurement zone.

Figure 4 shows the distorted droplet image. Overlaid on the droplet image is the outline of a 19.4-μm diameter droplet as calculated by the approach described above. Agreement between experiment and theory is excellent.

For comparison to oleic acid, Fig. 5 shows a water droplet of about the same size. The distortion is not as great as with oleic acid because of water's greater surface tension. This acceleration-induced distortion difference between oleic acid and water was noted in early experiments (Baron, 1986; Baron *et al.*, 1993).

5.2. *Droplet undersizing measurements*

When droplets are accelerated in the APS nozzle, they flatten as indicated in Figs 4 and 5. The flattening (perpendicular to the air flow) results in increased drag (in the direction of the airflow) and hence increased droplet velocity. The observation of a higher velocity for a particle is interpreted by the instrument as a smaller aerodynamic diameter. The droplets are therefore undersized. Results of early experiments on the undersizing of APS-measured oleic acid droplets have been published (Baron, 1986). Figure 6 compares experiment and theory regarding the distortion-induced undersizing. The original experimental data was not corrected for density and these corrections were made for the data in Fig. 6 (Wang and John, 1989).

Additional APS undersizing measurements using liquids with a range of viscosities and surface tensions were carried out as part of this study. Several measurements were made using polydimethyl-siloxane oils, designated DC 200 (Dow Corning, Midland, MI), that covered a range of viscosities. Table 1 lists the relevant properties for these oils.

Aerosol droplets were generated using a VOAG. The generator was operated in a pressure-feed mode from a reservoir with a pressure of approximately 88 kPa (Baron, 1986). The materials indicated in Table 1 (except water) were placed in a solution of heptane. The solution concentration was chosen to give nominal solute droplet diameters of 5, 7.5, 10, 12.5, and 15 μm. The droplet aerodynamic diameter was measured in a settling chamber (Wall *et al.*, 1985) and determined from the average particle settling velocity of at least 15 particles. Finally, the droplet sizes recorded by the APS were compared to the aerodynamic diameter as calculated from the settling velocity. Unlike calculation from the VOAC parameters, requiring knowledge of the droplet density, the settling velocity gives a direct indication of the aerodynamic diameter, since the airflow in the settling of small droplets is so small that droplet distortion is negligible.

The APS was calibrated using monodisperse latex particles in the 5–15-μm range (Bangs Laboratories, Fishers, IN). Repeat measurements of the calibration particles exhibited a standard deviation in the range of 0.02–0.09 μm depending on particle size. These errors represent limits to the accuracy of the APS measurements. Settling velocity measurements typically had standard deviations of 1–4% (range of 0–7.6%), resulting in aerodynamic diameter standard deviations on the order of 1–2%.

Problems were occasionally observed while obtaining APS-measured diameter shifts, indicating that droplet surface tension or perhaps viscosity was affected by impurities in the generation system. This was especially evident when changing solutions. In order to

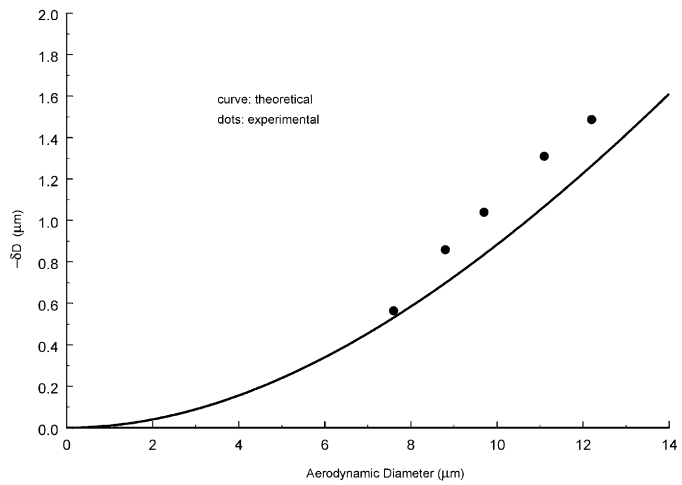

Fig. 6. Distortion-induced shift in the APS-measured diameter of oleic acid droplets. Data from Baron (1986). Solid curve is calculated using the theory presented here. $\delta D \equiv D_{\mathrm{APS}} - D_{\mathrm{aero}}$.

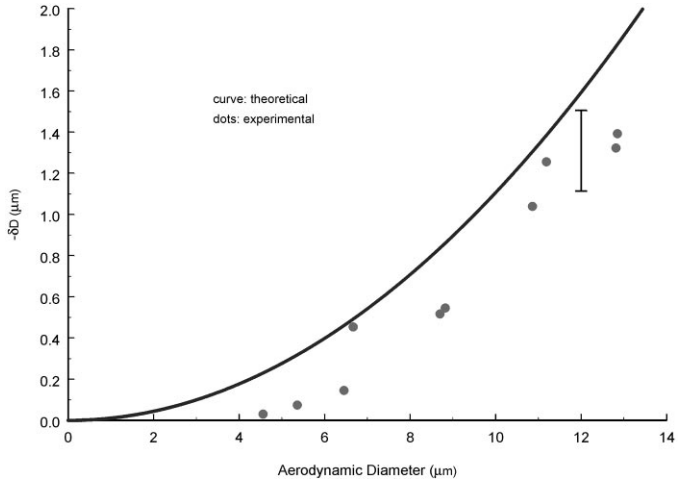

Fig. 7. Distortion-induced shift in APS-measured diameter of DC 200/50 oil droplets. $\delta D \equiv D_{\mathrm{APS}} - D_{\mathrm{aero}}$. Error bar represents 95% confidence limits on interpolated data mean.

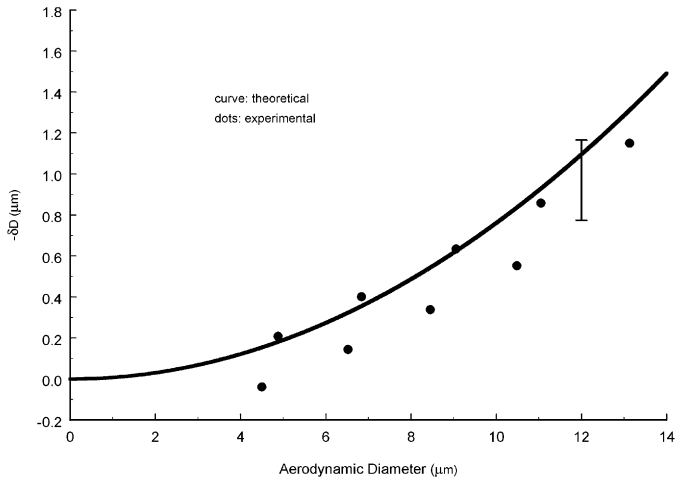

Fig. 8. Distortion-induced shift in APS-measured diameter of DC 200/100 oil droplets. $\delta D \equiv D_{\mathrm{APS}} - D_{\mathrm{aero}}$. Error bar represents 95% confidence limits on interpolated data mean. One data point has been omitted as an outlier.

account for this effect and the APS variability as well, two equivalent experiments separated by at least a month were carried out for each oil. Each experiment produced five data points each.

5.3. *Results*

The experimental results are shown together with computed values in Figs 7–10. Results are presented as the difference between the aerodynamic diameter (as calculated from the settling velocity) and the APS-measured particle diameter as a function of the aerodynamic diameter. The density-dependent diameter shift from (aerodynamic) diameter corresponding to a unit density particle is additional to the shift given in the figures. However, the density of the oils tested was sufficiently close to standard density (1000 kg m^{-3}) that the density correction was negligible ($<0.07\%$).

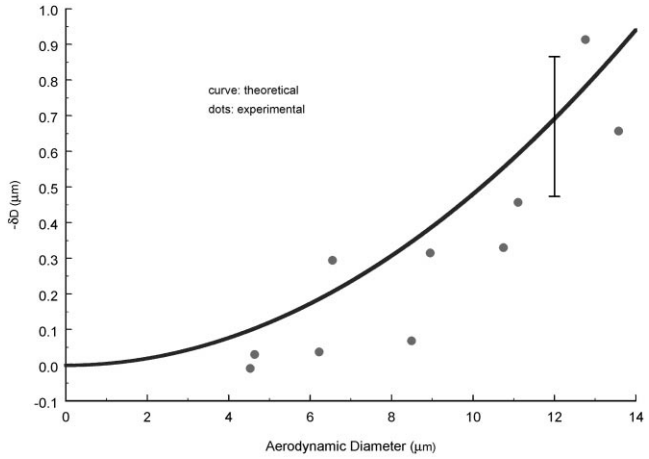

Fig. 9. Distortion-induced shift in APS-measured diameter of DC 200/200 oil. $\delta D \equiv D_{\mathrm{APS}} - D_{\mathrm{aero}}$. Error bar represents 95% confidence limits on interpolated data mean.

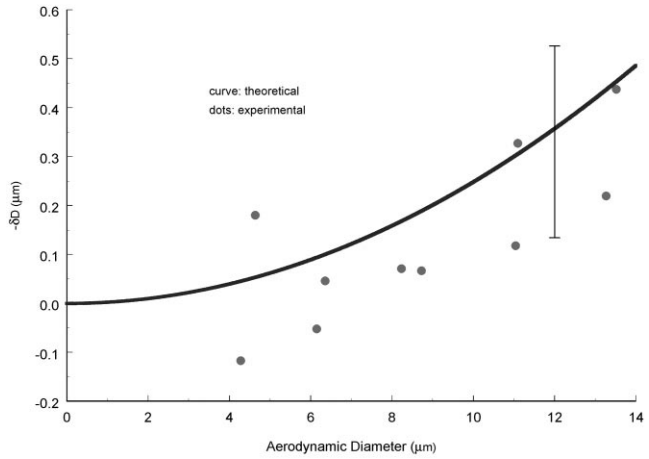

Fig. 10. Distortion-induced shift in APS-measured diameter of DC 200/500 oil $\delta D \equiv D_{\mathrm{APS}} - D_{\mathrm{aero}}$. Error bar represents 95% confidence limits on interpolated data mean.

The inter-experiment variability mentioned above was analyzed as a variance roughly constant over diameter. This feature is particularly visible in Fig. 8 where the inter-experiment bias was large relative to the inter-diameter variability so that the former is quite visible; alternate points correspond to the two different experiments. The inter-experiment variability was estimated by pooling the variances estimated from each oil, and is depicted in the figures using error bars about an interpolated data mean estimate at diameter chosen to equal 12 μm. The error bars give 95% confidence intervals (using Student t quantiles at four degrees of freedom). Note that the error bars depict an overall upwards or downwards shift in the data, rather than inter-diameter variance.

6. DISCUSSION/CONCLUSIONS

The theory given above is at once simple to apply and yet adequate at the least for qualitative interpretation. In fact, as can be observed in Figs 6–10, the calculated and measured diameter shifts are remarkably close, considering the simplifying assumptions in

the theory. With the more recent experiments shown in Figs 7–10, the calculated curves, falling mostly within the 95%-confidence limit bars, appear slightly high at the smallest viscosities (Figs 7 and 8). On the other hand, the data here appear to be approaching negative values at small diameters and may therefore be slightly low. Furthermore, the calculated shifts appear somewhat *small* relative to the earlier experiment with oleic acid (Fig. 6). Overall, then, the theory appears consistent with experiment. Further evidence for the adequacy of the theory is provided by the agreement between calculated and experimental laser images of droplet shapes (Fig. 4).

Though we would not conclude that the theory has been *verified*, the consistency found provides justification for expansion on this work. Uncertainties in both experiment and theory can be narrowed. In particular, the theory presented here was developed on the basis of small perturbations from spherical shape and cannot be considered reliable in giving details of the shape when the distortion is large. Higher-order corrections to the theory could be examined in order to obtain quantitative estimates as to their significance. Particularly intriguing is the possibility of drag-induced circulation (Clift *et al*., 1978, p. 35) within the droplets. Associated with circulation is a possible asymmetry in the droplet shape, up vs downstream. Although such circulation has not yet been observed with small droplets, experiments to date have not dealt with the large acceleration achieved in the APS nozzle. Nevertheless, the computed velocities may depend mainly on gross features of the droplet shape, and it may be found that they are insensitive to such assymetries.

Additional experimentation may help sort out other important features of droplet distortion and its effect on motion. Calculation indicates that aerosols, such as water droplets, with large β (equation (1)) are capable of oscillating. Such oscillation may be found to be excitable by accelerating air in nozzles other than the APS'. Aside from oscillation, the response of high-β aerosols to accelerating flow may, however, be characteristic in other ways. Unfortunately, experiments with such materials may be difficult, since large β tends to correlate with high vapor pressures, so that rapid droplet evaporation may complicate measurement. Aerosols with β close to the critical value of 1.7, signaling the onset of overdamped (non-oscillatory) relaxation, may also exhibit specific characteristics worth investigating.

Another worthwhile endeavor would be to explain the inter-experiment variability found. Perhaps the details can be uncovered as to how impurities affect results. In the meantime, with the variations noted above in ostensibly pure substances, liquid test aerosols should be used cautiously.

Further experimentation with liquids of different surface tensions and viscosities and with other nozzle designs are needed to confirm the various features of the theoretical model presented here. Considerable modification in the theory may be necessary, especially with supersonic air flows as in the Aerosizer. Theory should then provide insight into developing a much-simplified empirical model for real-time correction of aerosol size measurements for distortion effects, assuming that such properties as the surface tension, viscosity and density are known accurately.

Acknowledgements—We wish to thank Dow Corning Corporation, Midland, MI for providing samples of the polydimethyl-siloxane oils.

REFERENCES

Abramowitz, M. and Stegun, I. A. (eds) (1965) *Handbook of Mathematical Functions*. Dover Publications, Inc, New York.

Ananth, G. and Wilson, J. C. (1988) Theoretical analysis of the performance of the TSI aerodynamic particle sizer: the effect of density on response. *Aerosol Sci. Technol.* **9**(3), 189–200.

Baron, P. A. (1986) Calibration and use of the aerodynamic particle sizer (APS 3300). *Aerosol Sci. Technol.* **5**, 55–67.

Baron, P. A., Mazumder, M. K. and Cheng, Y. S. (1993) Direct reading techniques using optical particle detection. In *Aerosol Measurement*: *Principles*, *Techniques and Applications* (Edited by Willeke, K. and Baron, P. A.), pp. 381–409. Van Nostrand Reinhold, New York.

Clift, R., Grace, J. R. and Weber, M. E. (1978) *Bubbles*, *Drops*, *and Particles*. Academic Press, Inc, Boston.

Fuchs, N. A. (1964) *The Mechanics of Aerosols*. Pergamon Press, Oxford.

Griffiths, W. D., Iles, P. J. and Vaughan, N. P. (1986) The behaviour of liquid droplet aerosols in an APS 3300. *J. Aerosol Sci.* **17**(6), 921–930.
Ho, J. (1996) Real time detection of biological aerosols with fluorescence aerodynamic particle sizer (FLAPS). *J. Aerosol Sci.* (Suppl. 1) **27,** S581–S582.
Landau, L. D. and Lifshitz, E. M. (1959) *Fluid Mechanics*. Pergamon Press, London.
Lamb, H. (1945) *Hydrodynamics*. Dover Publications, New York.
Madelin, T. M. and Johnson, H. E. (1992) Fungal and actinomycete spore aerosols measured at different humidities with an aerodynamic particle sizer. *J. Appl. Bacteriol.* **72**(5), 400–409.
Maynard, A. D. and Kenny, L. C. (1995) Performance assessment of three personal cyclone models, using an aerodynamic particle sizer. *J. Aerosol Sci.* **26**(4), 671–684.
Schlichting, H. (1979) *Boundary-Layer Theory*. McGraw-Hill, New York.
Sioutas, C., Abt, E., Wolfson, J. M. and Koutrakis, P. (1999) Evaluation of measurement performance of the scanning mobility particle sizer and aerodynamic particle sizer. *Aerosol Sci. Technol.* **30**(1), 84–92.
Wall, S., John, W. and Rodgers, D. (1985) Laser settling velocimeter: aerodynamic size measurements on large particles. *Aerosol Sci. Technol.* **4**(1), 81–87.
Wang, H.-C. and John, W. (1989) A simple iteration procedure to correct for the density effect in the aerodynamic particle sizer. *Aerosol Sci. Technol.* **10**(3), 501–505.